Chapter 3
Nanomaterials Behavior under Irradiation Impact

Abstract In this chapter, the main attention is given to the possible effects of irradiation on the structure and properties of NMs. The data on various nanostructures behavior under irradiation by high energy ions/neutrons as well as the possibilities and potentialities of some microscopic approaches and MD modeling results are considered and generalized. The examples of possible practical use of NMs are presented and several poorly investigated problems are discussed.

3.1 General Considerations

A very important role of various materials in the general nuclear industry progress is well known, and it is reasonable to consider the use of namely NMs in this field, especially bearing in mind their stability under irradiation, with accounting the temperature, loadings, corrosive media action, etc. Let us remember a general picture of the origin of radiation defects in a solid body during radiation. As a rule, it is suggested that under irradiation by high energy ions and neutrons, there is observed a partial energy transfer to the displaced atoms of crystalline lattice, which leads to the formation of primary knocked-out atoms (PKA). That process generates so-called displacement cascades containing the Frenkel pairs in the form of both interstitial atoms and vacancies (IAV) and their complexes (clusters) in the form of vacancy loops (or vacancy nanopores) as well as dislocations. The point radiation defects can collide (and annihilate) both at meeting each other and/or after moving further apart along GBs, which in such a situation act as sinks for radiation defects. An intense irradiation of material leads to the following general effects influencing the material structure, content, and properties: material amorphization; plasticity decrease or embrittlement (this effect has been long known in material science and called as radiation hardening); high-temperature creep growth; intensification of boundary segregation processes; material swelling as a result of the non-compensated vacancy and atomic sinks; surface blistering under ion irradiation, and elements transmutation owing to some nuclear reactions and decays.

R.A. Andrievski and A.V. Khatchoyan, *Nanomaterials in Extreme Environments*,
Springer Series in Materials Science 230, DOI 10.1007/978-3-319-25331-2_3

Compared to traditional CG materials (e.g., [1]), information, concerning the generation of radiation defects, their development and properties in various NMs, is very poor since many of these studies are still in their infancy (e.g., [2–7]). It is obvious that the presence of the developed interface system in NMs must increase its role as radiation defects sinks (as compared to the CG counterparts), and so the negative action of radiation effects can be attenuated. However, on the other hand, such accumulation of radiation defects at GBs can initiate nanostructure amorphization processes during which the displacement cascade development has its own specificity in macro- and nanostructures. It is important that in such situation, we cannot unambiguously estimate the positive and negative influences of the irradiation action. From the given general considerations and the available data, at least, four different versions of the NMs behavior under irradiation can be distinguished:

(1) In the NMs with a developed system of various interfaces (such as GBs and TJs) performing the role of radiation defect sinks, the radiation resistance increase is observed in comparison with their traditional CG counterparts.
(2) In some NMs, irradiation can promote annihilation of nanostructures and thus leads to the transformation of them into an amorphous state.
(3) The presence of radiation defects can generate or stimulate various recrystallization processes, which can influence the two above described versions of material transformation.
(4) Finally, transmutation processes should be taken into account, especially in the case of irradiated fuels and boron-containing materials (for example, in the latter case, due to (n, α) reactions the materials are depleted of boron and demonstrate swelling caused by helium accumulation in pores).

Besides, one must distinct the complicated peculiarities of the behavior of various samples under irradiation (bulk specimens and thin films, objects with metallic and covalent bonds, etc.) as well as different penetration ability of ions and neutrons in materials under study. Thus, the problem the NMs behavior under irradiation requires the consideration of many factors.

3.2 Main Experimental Results

3.2.1 Ion Irradiation

The ion irradiation in accelerators cannot trace all the features of radiation defects behavior, but this approach is widely used in the current experimental practice thanks to its economic and operative advantages in comparison with the so-called reactor experiments. Investigations of the effect of ion implantation on the material properties started in the 80th of last century (see survey [8]), but systematic studies in the NMs field (especially with accounting the GS effect) have been carried out

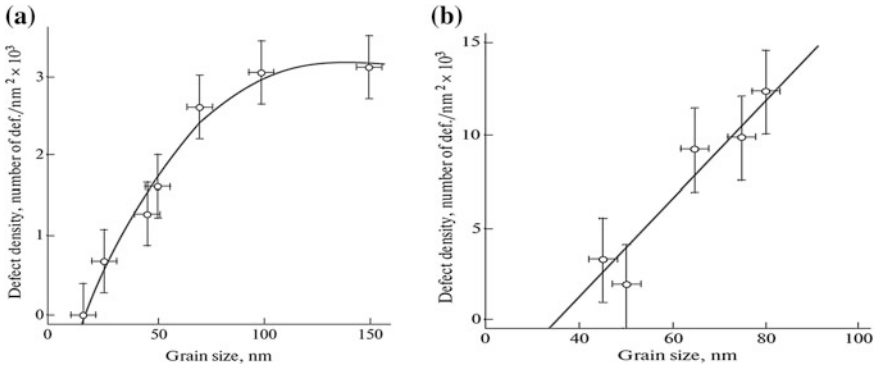

Fig. 3.1 The GS effect on the radiation defect density in zirconium oxide samples (**a**) and palladium those (**b**) irradiated with Kr ions at 293 K (ZrO_2: energy E = 4 MeV according to dose of 3–8 displacements pear atom (dpa); Pd: E = 0.24 MeV according to dose of 110–210 dpa) (adapted from [2])

only over about 20 years, and the first such results were presented at the Second International Nanomaterials Conference NANO1994 in Stuttgart [2, 9]. Figure 3.1 shows the radiation defect density changes due to irradiation of ZrO_2 and Pd samples. One can see that there is a marked decrease in the radiation defect density for the sizes ranging from 100–150 to 20–40 nm. At a grain size below 15 nm (ZrO_2) and 30 nm (Pd), defects in irradiated samples were not observed at all [2, 9], which indicates an elevated radiation stability of nanostructures.

By now, other authors have confirmed the conclusions [2, 9]. Some characteristic and interesting results obtained over 2004–2014 are presented in Table 3.1 with short description of methods for sample preparation and the irradiation conditions. The presented data convincingly indicate that practically in all studied materials, such as metals, alloys, steels, intermetallic compounds, and oxides, prepared by various nanotechnology methods, the nanostructures turned out to be more resistant to ion irradiation compared to the microstructures in their traditional CG counterparts.

In addition, it should be marked that numerous and demonstrative results, which were obtained in experiments with multi-layer films, can be added to Table 3.1. The interlayers in such systems serve as sinks radiation defects. Using layers with non-miscible components and varying their individual thicknesses so that the summed film thickness can remain constant, one can easily trace the influence of the number of individual layers on the material microhardness, swelling and other characteristics under irradiation. An illustrative example is presented in Fig. 3.2, where changes in the radiation hardening (a) and swelling (b) for some multi-layer Cu/V films are presented as functions of the reciprocal values of the individual layer thicknesses. The results descriptively show that the thinner individual layers in a film (i.e., the greater the number of interfaces acting as sinks for radiation defects), the smaller the increase in its hardness and helium pores formation.

Table 3.1 Effect of ion irradiation on NMs

Materials and manufacturing method	Grain size L (nm)	Conditions of irradiation				Main result
		Ion	E (MeV	Dose Fluence (dpa) (ion/m^2)	T K	
Ni (electrodeposition)	20–30	Ni	0.84	5	293	No change in L was registered; the SFT formation was observed
Ni (HPT)	115	Proton	0.59	0.56	293	L decreased to 38 nm; SFT and twinned boundaries (TBs) were formed; hardness increased in about 2 times
Cu–0.5Al_2O_3(HPT) [10, 11]	~180	Proton	0.59	0.91	293	L increased to 495 nm; SFT are formed; hardness remained unaltered. In all cases, the radiation- induced SFT density in NMs was smaller than that in CG materials
$MgCa_2O_4$ (consolidation at 5 GPa) [12]	4–12	Kr	0.3	12–96	100	Amorphization was not observed. Amorphization started at 12 dpa (at L >1 μm)
TiNi (HPT) [13]	31 ± 6	Ar	1.5	0.2–5.6	293	Amorphization was not observed. Amorphization started at 0.4-2.5 dpa (at L >100 μm)
W–0.5TiC (hot isostatic pressing (HIP) [14]	50–200	He	3	2×10^{23}	823	Critical fluence for blistering is tenfold that of CG samples
UFG–316SS austenitic steel (HPT) [15]	40	Fe	0.16 10	10 10	623	Radiation-induced segregations at GBs are smaller in nanosteel
Fe film (magnetron sputtering) [16]	49–96	He	0.1	6×10^{20}	293	The density of He bubbles and radiation hardening are smaller in nanofilms
14YWT ferritic steel (hot extrusion and rolling HE/R) [17]	L = 200–400; nano-clusters of 1–5	Pt	10	15–160	173–1023	The main beneficial features of nanostructure remain almost unchanged after irradiation at all studied conditions

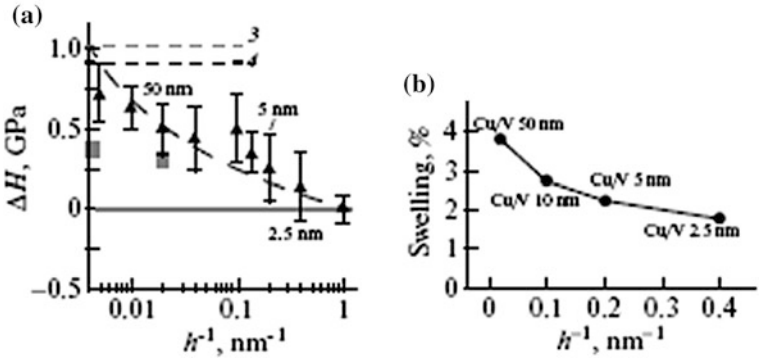

Fig. 3.2 The radiation hardening (**a**) and swelling (**b**) as a function of the reciprocal thickness of one layer in Cu/V multi-layer films irradiated with He ions (E = 50 keV; fluence of 6×10^{20} m^{-2}; T = 20 °C). Lines 3 and 4 (**a**) relate to the ΔH for Cu and V individual films, correspondingly [18]

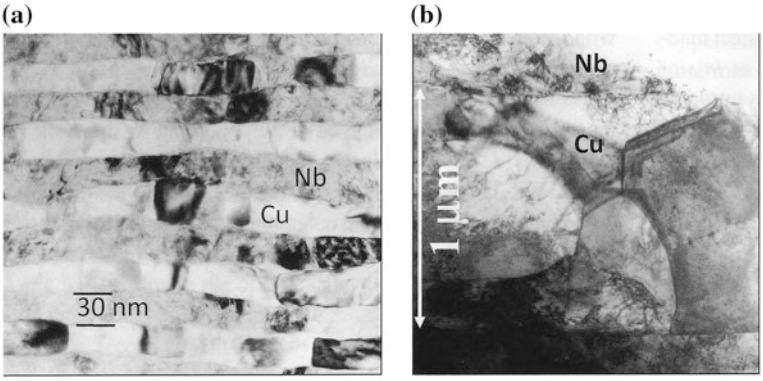

Fig. 3.3 TEM images of rolled multi-layer Cu/Nb samples with different one layer thickness (h) after an irradiation with He ions (E = 0.15 MeV; fluence of 10^{21} m^{-2}; T = 20 °C): **a** h = 30 nm; **b** h = 1 μm (adapted from [19])

In general, the presence of thin individual layers promotes preservation of a layered morphology after irradiation, which is conveniently illustrated for the Cu/Nb films in Fig. 3.3, where in the case of thin individual layers (a) a nanolaminated structure remains after radiation without any evidence to the presence of dislocation defects, which radically differ from the thick-layer system behavior (b), where we see characteristic disorders of the layers, dislocation-cell structures, and even some marks of grain rotation. Analogous results demonstrating a similar role of such thin individual layers under irradiation were obtained by many authors for other various multi-layer films (Cu/W, W/ZrO_2, Ta/Ti, Ag/Ni, CrN/AlTiN, etc. [20–24]), where in some cases the interfaces are not purely metallic but mixed (metal-oxide) and nitride ones.

A more complicated situation is observed in the case of irradiation of the nanostructured wide-zone semiconductor β-SiC (3C-SiC), a very interesting material not only for nuclear industry, but also for nanoelectronics, chemical technology, and some biomedicine applications [25, 26]. It is known from literature that the β-SiC nanostructure is tolerant to the irradiation with 4 MeV Au ions [27] and, in contrary, the behavior of irradiated nanostructured samples (L = 30–50 nm) and single crystals looks much the same [28, 29]. However, a more detailed following study of nanostructured β-SiC films and single crystals, irradiated with 0.55 MeV Si ions, has shown that at room temperatures the total amorphization of these objects occurs at irradiation dozes of ~3 and ~0.29 dpa, correspondingly [30]. Such preferential nanostructure tolerance is connected with a high density of planar defects (in the form of stacking faults), which promote the IAV recombination processes leading to self-healing of the generated radiation defects. The following TEM in situ examination of electron irradiated silicon carbide films confirmed the important role of planar defects acting namely as sinks and traps in the IAV processes [31].

The features of irradiation induced amorphization in some nanostructures can be illustrated by the results of the nanoparticles behavior studies in inert SiO_2 matrices presented in Table 3.2.

Particularly representative results were obtained for zirconium oxide: ZrO_2 nanoparticles amorphizate under the action of a moderate irradiation doze with Xe ions, whereas the oxide single crystal preserves its crystal state even at high irradiation dozes. As shown in Table 3.2, the dimension-size effects are observed for Cu and Ge, but Au nanoparticles do not amorphizate in the studied size range. The

Table 3.2 Irradiation effect on nanoparticles embedded in amorphous silica (SiO_2)

Subject	Size of nanocrystal (nm)	Irradiation conditions			Main result
		Ion	E (MeV)	Dose (dpa) Fluence (ions/m^2)	
ZrO_2/SiO_2 [32] ZrO_2 [33]	~3	Xe	1	~0.8	Amorphization
	Single crystal	Xe	0.4	680	Preservation of crystal state
Cu/SiO_2 [34, 35]	~2.5	Sn	5	0.16	Amorphization
	~8	Sn	5	10^{19}	Preservation of crystal state
Au/SiO_2 [32, 36]	3	Xe	1	~0.8	Preservation of crystal state
	3–5	Sn	2.3	10^{19-20}	Preservation of crystal state
Ge/SiO_2 [37, 38]	4–8	Si	5	10^{15-19}	Amorphization of nanocrystals is observed firstly
Co/SiO_2 [39]	3.7 ± 1.0	Au	9	10^{17}	Amorphization

problem of the nanoparticles behavior is complicated, and readers can find more detailed information in review [40]. Especially for the oxides irradiation by fast neutrons, it was shown that a spontaneous radiation amorphization starts at some critical defect concentration when the ions displacement ranges up to the value known as the Lindemann melting criterion [41], but in general, the problems of size effects in such systems remain to be solved.

It must be marked that the studies of the ion irradiation influence on the NMs structure and properties offer contradicted experimental results, and thus scientists come up against complex and non-ordinary problems requiring modern techniques or combination of the available ones. Now, in the field, there are many diverse and independent modern methods, such as TEM (including high-resolution variant HRTEM), scanning electron microscopy (SEM including high-resolution variant HRSEM), XRD methods, including small-angle X-ray scattering, glancing-incident angle X-ray diffraction (GIAXRD), extended X-ray absorption fine structure spectroscopy, X-ray absorption near-edge spectroscopy, energy dispersive spectroscopy (EDS), selected area electron diffraction (SAED), Rutherford backscattering spectrometry, Auger electron spectroscopy, electron backscattering diffraction (EBSD), atom probe tomography (APT), differential thermal analysis/thermal gravimetric analysis (DTA/TGA), atomic force microscopy, Raman spectroscopy as well as improved or advanced micro/nanoindentation tests and electrical/magnetic measurements. For theoretical considerations and estimations, there were elaborated some new modeling methods, and now ion penetration and irradiation damage profiles can be calculated with the use of the known software stopping and range of ions in matter (SRIM) program. As an example, the calculated damage and implantation profiles are presented in Fig. 3.4 for β-SiC samples (with GS of 30–50 nm) irradiated with 4 MeV Au ions (adapted from [29]).

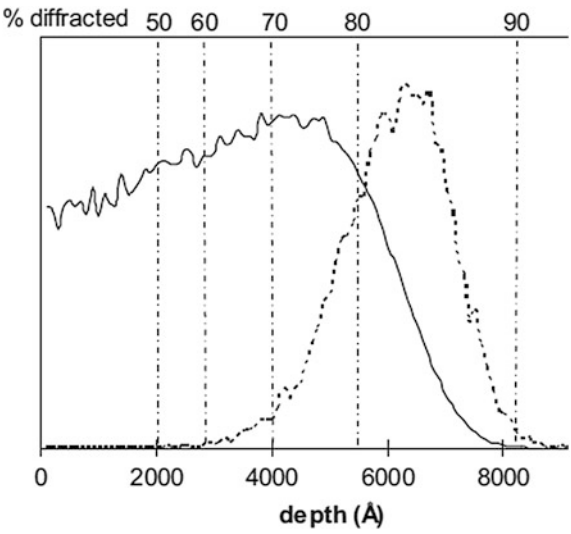

Fig. 3.4 The damage profile in SiC (*continuous line*) and Au implantation profile (*dotted line*)

On the upper line of Fig. 3.4, the depth of the diffraction measurements by GIAXRD is presented in %, and the results allow one to make a conclusion that about 80 % of the irradiation depth can be connected with the damage region and about 20 % relates to the mixed zone (implantation + damage). Such estimations can be important for analysis of changes in the NMs properties under an ion irradiation.

Besides the above presented data on the NMs tolerance to irradiation and their possible amorphization, there are some other listed below interesting results waiting for consideration and interpretation.

1. The studies of the GG in nanostructured metallic films (Au, Pt, Cu, Zr, and Zr–Fe), exposed to irradiation with Ar ($E = 0.5$ MeV) and Kr ($E = 0.5$–1 MeV) ions [42], have shown that there are three distinct ranges related to temperature: a purely thermal one (where temperature is a dominant factor of GG), thermally induced or mixed (where thermal and radiation effects are summarized), and low-temperature one (where the thermal effect on GG is very weak). The temperatures of transitions from mixed to low-temperature ranges depend on the object under study, but they oscillate by the homological temperature scale between 0.15 and 0.20 T_m. Based on these data, a theory of radiation-induced GG was developed supposing some thermal peaks formation under irradiation in cascades and subcascades. In the frame of this theory, the radiation-induced grain growth can be described by the expression

$$L^n - L_o^n \sim K\Phi t, \tag{3.1}$$

where $n \sim 3$, Φ is the ion beam intensity (ion/m^2 s), t is the time, K is a constant dependent on the grain mobility and moving force, L and L_o correspond to the moving and initial values of the GS.

2. For nickel and copper, the growth of the radiation defects number with increasing the irradiation was detected especially for samples having the SFT (with a mean size of 2.5–4.4 nm) and TB forms [10, 11]. It is interesting that in Ni, this dependence is accompanied by decrease in GS from 115 nm down to 38 nm, whereas by contrast in copper, the size growth from 178 to 493 nm was observed. The authors [11] especially marked this fact and underlined that such distinction needs the further studies and considerations. The mean GS increase from 40 to 60 nm was also observed in nanostructured austenitic steel 316SS irradiated with 0.16 MeV Fe ions [43]. The sufficient difference in the nanograin growth rates was shown [44] for the tetragonal and cubic ZrO_2 crystal modifications irradiated with Kr ions ($E = 0.34$ MeV).
3. The radiation induced processes and their role in the GBs enrichment/depletion with different elements (as well as the chromic steels reinforcement by some nanoinclusions) were widely and fruitfully investigated in several works, where the combination of TEM, EBSD and APT methods was used (e.g., [45, 46]). As an example, Fig. 3.5 demonstrates the evolution of oxide nanoinclusions

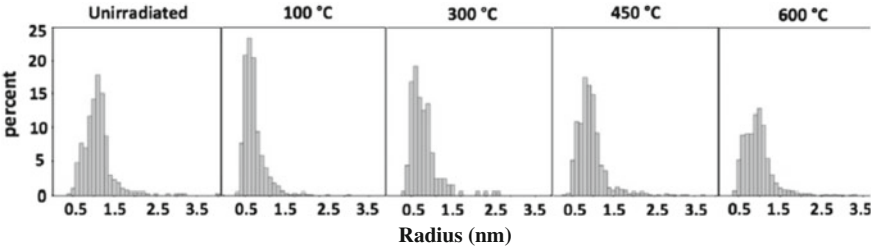

Fig. 3.5 TEM data concerning the irradiation temperature effect on the oxide nanoinclusion distribution histograms after irradiation of 14 YWT steel with Ni ions (adapted from [46])

(Fe, Ti, Y)O_X for the 14YWT steel samples irradiated with Ni ions (E = 5 MeV, dose of 100 dpa). From the other side, there were obtained element distribution maps for some nanostructures [46]. Naturally, such data are important for estimation of changes in the mechanical and corrosion properties of widely used alloyed steels after irradiation.

4. The high-temperature strength and creep of copper and its alloys under irradiation with Kr ions (E = 1.8 MeV, dose up to 75–100 dpa) were studied by Averback et al. [47, 48], and it was found that a marked growth of high-temperature inclusions begins at temperatures $\sim$0.65 and $\sim$0.85 T_m (corresponding to the Mo and W additions). The dependence of the creep velocity on the stress and irradiation dose proved to be linear.
5. In porous samples, the open pores surface rise is favoring to the removal of radiation defects, i.e., if the sinks number growth is increasing, then such porous objects increases their radiation stability as compared with usual dense samples. This phenomena was been clearly demonstrated for the irradiated porous samples of ZrO_2 [49] and Au [50].
6. In the works of Yu, Zhang et al. [24, 51–53], the methods of HRTEM (including in situ studies of irradiation-induced objects), XRD, and SAED revealed the TBs properties as sinks of radiation defects. The studies of interfaces in multi-layer films of Ag/Ni, Ag/Al, Cu/Fe, and Cu/Ni types allow formulating the following two main criteria of the TBs formation in the described FCC metal structures: a low value of the TBs energy and their high coherence.
7. In Fig. 3.6, radiation damages are compared for single crystal (SC), CG (L = 20–30 μm), and nanocrystal grain (NG) copper samples irradiated with He ions. The results show marked distinctions in both the number and sizes of radiation pores in samples with different GS. At the same time, it was detected that in single crystal samples (with initial mean GS of $\sim$15 nm) the radiation-induced defects are smaller and preferentially oriented along the GBs (the mean GS in irradiated NG samples was $\sim$35 nm).
8. In nanocrystalline W films under irradiation by Au ions (E = 4 MeV; dose range from 6 to 100 dpa) at radiation doses over 30 dpa, the transformation of the primitive cubic phase (β) into the BCC modification (α-phase) was observed [55].

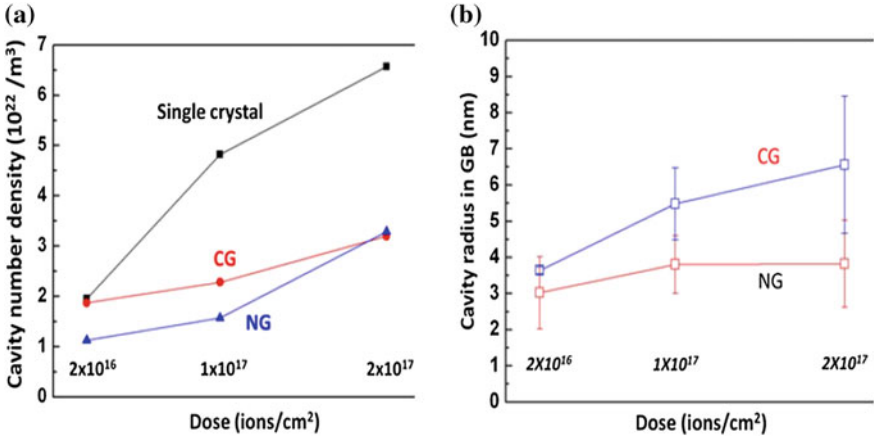

Fig. 3.6 The dose effect on the cavity number density (**a**) and cavity radius (**b**) in single crystal, CG, and NG Cu samples after irradiation with He ions at 450 °C (adapted from [54])

From the other side, the irradiation leads to the GS growth from ~13 to ~19 nm, which corresponds to the above mentioned expression (3.1) which was put forward in [42].

3.2.2 Neutron Irradiation

The positive role of nanostructures in the material radiation stability growth, revealed in the experiments with ion irradiation [2, 3, 9–13], on the one hand, initiated the reactor tests of various NMs and, on the other hand, became a base for some new nanostructured steels development, specially designed to be used in fission and fusion reactors of the IV generation. Table 3.3 lists the main results concerning the considered NMs structures and the properties changes initiated by neutron irradiation.

These data make it is obvious that a GS decrease practically always raises the material radiation stability, just as it was observed in the ion irradiation tests (see Table 3.1). At the same time, it should be marked that the number of reactor tests and their duration remain limited and general information concerning the behavior of materials with small nanograins (below 100 nm) under the real conditions of reactor operational regimes seems to be absent. The problems are connected with both the difficulties of the reactor tests themselves and the deficiency of the required bulk NMs.

The effectiveness and advantages of the described radiation studies in general can be illustrated by the presented in Table 3.4 results obtained in comparative tests carried out especially for two types of the structural steels, namely, the CG steel ODS-EUROFER (developed in West Europe) and new nanostructured steel

Table 3.3 Effect of neutron irradiation on NMs and some materials with related structure (oxide dispersion-strengthened (ODS) steel (CVD means chemical vapor deposition; CVI does chemically vapor-infiltrated)

Material (manufacturing)	Grain size (nm)	Conditions of irradiation			Main result
		E (MeV)	Dose (dpa) Fluence (n/m^2)	T (K)	
Modified ferritic/martensitic ODS 9–12Cr steels (HE/R) [56]	10^3–10^4(grains); ~4 (inclusions)	>0.1	15	670–807	The size and content of nanoinclusions (near $Y_2Ti_2O_7$) retain stability
UFG SUS316L + 1 %TiC (HIP and rolling); Ni (electrodeposition); Ni–W (the same) [57]	100–300; 650	>1	10^{23}–10^{24}	560	Small or no increase hardness was observed after irradiation
W–0.5TiC (HIP) [14]	50–200	>1	2×10^{24}	873	Radiation hardening and defects were smaller in nano W
Austenitic UFG-CW 316SS (HPT) [58]	40; 40×10^3	>1	12	633	Decreasing GS results in more precise the segregation study
Nanostructured ferritic steel 14YWT (HE/R) [59–61]	100–300 (grains); 1–4 (inclusions)	>0.1	1.2–1.6	573–973	Small radiation hardening and plasticity some decrease
Nanostructured ferriticsteel MA957 (HE/R) [62]	1200/300 (ℓ/L)	>0.1	3	873	The size (~2 nm) and content of nanoinclusions (Y–Ti–O) retain stability
SiC and its composites SiC/SiC (CVD and CVI) [63]	10^4–10^5	>0.1	~28 40.7	573, 923 1073	Swelling, thermal conductivity and strength have been studied in detail. Irradiation-insensitivity was demonstrated
Austenitic AISI 321 steel (ECAP) [64]	300–400; 40×10^3	>1	5.3	293–623	Radiation hardening and plasticity decrease are smaller after ECAP
UFG low carbon steel (ECAP) [65]	370 ± 60; ~44×10^3	>1	1.15×10^{-3}	328	Irradiation hardening and ductility decrease were smaller after ECAP
Creep of nanopowder sintered SiC (sintering additions and hot pressing) [66]	216, 414	>0.1	1.9	653–1453	The effect of GS and irradiation was studied and discussed

Table 3.4 Yield strength (σ_Y), ultimate tensile strength (σ_{UTS}), total elongation (δ), fracture toughness (K_{IC}), temperature of brittle to ductile transition (T_{BDT}), and difference of T_{BDT} (ΔT_{BDT}) for ODS-EUROFER and 14YWT steels in initial and neutron-irradiated ($E > 0.1$ MeV, dose of 1.5 dpa, and $T = 300$ °C) states

Steel	State	σ_Y (MPa)	σ_{UTS} (MPa)	δ (%)	K_{IC} (MPa $m^{0.5}$)	T_{BDT} (° C)	ΔT_{BDT}
ODS-EUROFER	Initial	966	1085	11.7	160	–115	85
	Irradiated	1243	1254	7.1	180	–30	
14YWT	Initial	1435	1564	12.0	175	–188	12
	Irradiated	1560	1641	7.4	225	–176	

14YWT, offered by Oak Ridge National Laboratory (USA) and developed on the modern approaches in the field [60]. These results testify the higher mechanical properties of the 14YWT steel in both the initial and irradiated states. Of special interest are the facts of sufficiently less radiation hardening and the temperature shift (ΔT_{BDT}) in irradiated samples for the transition from a brittle state to a ductile one. These advantages must be connected namely with a 14YWT steel structure, including the elongated grains (with length to 1–1.5 μm and mean width ~300 nm) and oxide inclusions with sizes of ~1–2 nm (see Fig. 3.5), that is markedly less than the ODS-EUROFER steel structural parameters. Besides, the nanoinclusions density in 14YWT steel is $\sim 2 \times 10^{24}$ m^{-3} and their characteristic features are a high coherence with the matrix phase and lower probability of the concentration stresses occurrence and, as a corresponding result, the nanocracks generation.

The thermal conductivity and swelling evolutions in SiC fibers, irradiated with fast neutrons ($E > 0.1$ MeV), are presented in Fig. 3.7, and it is easy to see that curves, describing two these characteristics behavior (a thermal conductivity decrease and a swelling increase) are stabilizing at an irradiation dose about 0.1–1 dpa. This level is wholly satisfactory one, and the studied materials (SiC fibers and impregnated SiC/SiC composites) can be considered as the radiation-resistive materials at least in the studied ranges of the neutron irradiation conditions (doses of 30–40 dpa, $T = 300$–800 °C). It should be marked that under these conditions the material mechanical properties are scarcely affected by irradiation, and the effect manifests itself only in the increase statistical spread of strength parameters, that is reflecting in a general characters of the so-called Weibull's relationships.

It is worthy to mention that in more complex systems the dependence of the material properties on the irradiation dose can have a more complicated character. For example, the studies of SiC samples sintered from the nanopowders with some activating additives have shown that irradiation elevates the creep velocity as well, but the GS effect manifests itself only in the 226–414 nm GS interval and at low radiation dozes (0.011–0.11 dpa) [66]. For the fibers with CG structure ($L = 5$–10 μm), irradiation also elevates the creep velocity, but herein the GS effect is not observed in the 380–540 °C range and becomes detectable only at $T = 760$–790 °C. The radiation creep of the sintered SiC samples in the described condition is about 1.4–1.8 times greater than that for the fibers with a CG structure.

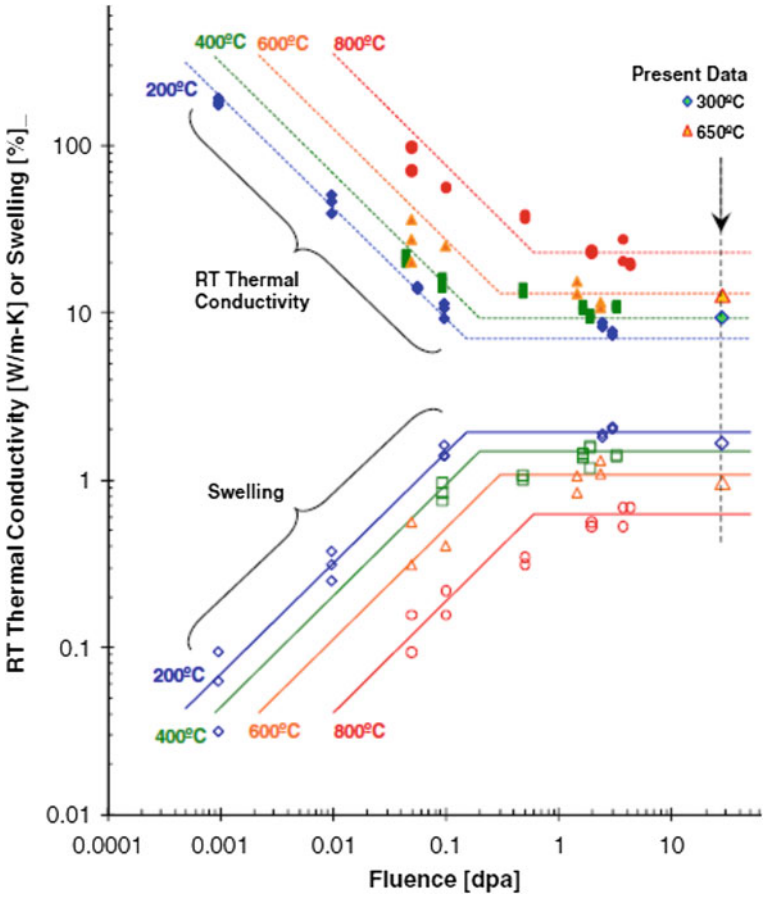

Fig. 3.7 Neutron fluence effect on thermal conductivity and swelling of CVD SiC (adapted from [63])

3.3 Some Theoretical Approaches and Modeling

A theoretical model describing a radiation-induced amorphization process in nanostructured objects was proposed by Ovid'ko and Sheinerman [67]. In this model, the Frenkel pairs IAV generation was suggested in two versions, namely for the high- and low-energy interactions separately. In the former case, the IAV pairs arise both at nano GBs and inside grains, whereas in the latter case, the vacancies come into being only at the GBs but interstitial atoms arise in nanograins. The evolution of radiation defects was theoretically analyzed for the following main stages: (1) generation of radiation-induced defects; (2) absorption of the defects by interfaces; (3) annihilation of IAV pairs; (4) formation of some stable clusters from point defects. For the high-energy interactions, stages (1) and (2) were considered

as dominating ones. Herein, a preferential amorphization region (dependent on the nano GS) was defined on the basis of the energy consideration, where the sum of the energies of interface surfaces and point defects elastic energies exceeds the energy of a characteristic threshold for the crystal-to-amorphous state transition. The developed interface net, on the one hand, assists the system free energy increase (i.e., decreases the energetic barrier of amorphization), but, on the other hand, favors to the radiation defects release, i.e., acts against the amorphization and enhances the NMs radiation stability.

A similar energy-based approach was developed by Shen [68], where the author proposed a qualitative model for the ΔG change depending on the GS and made an important conclusion that for every material there is an optimal interval of the GS, where radiation defects release and consequently amorphization resistance can be provided. This approach is schematically presented in Fig. 3.8 (adapted from [68]), where five energetic zones with different processes and characteristics may be defined:

1. Transition to an amorphous state is possible without any irradiation ($L < L_1$);
2. Transition to an amorphous state is initiated by a weak irradiation ($L_1 < L < L_2$);
3. Irradiation cannot lead to amorphization ($L_2 < L < L_3$);
4. Irradiation leads to amorphization ($L_3 < L < L_4$);
5. In this interval, where the GS exceeds L_4, the ΔG_{pd} value becomes more and more prevailing as with GS growth the interfaces reduce and the role of inter-grain boundaries in the radiation defects release falls off. At some L_m value, the annihilation of defects by the volume recombination mechanism becomes predominant.

The processes in zones 1, 4 and 5 are qualitatively confirmed by the experimental data (e.g., see Fig. 3.1). Some peculiarities of the radiation defects formation in nanocrystals imbedded into a solid matrix were studied by Oksengendler et al. [69].

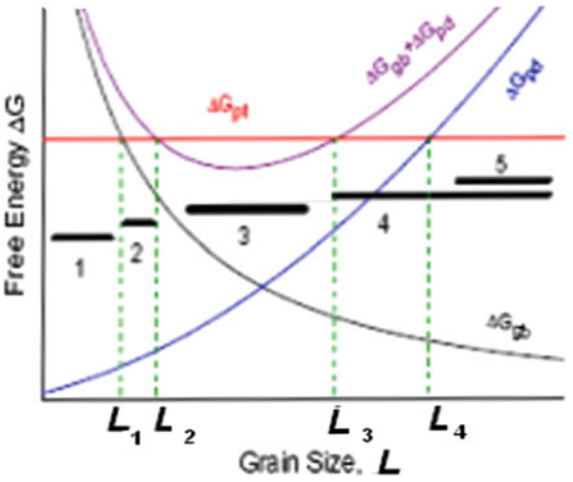

Fig. 3.8 Scheme of the GS effect on the free GB energy (ΔG_{gb}), free energy of point defect (ΔG_{pd}), their sum ($\Delta G_{gb} + \Delta G_{pd}$), and crystal-to-amorphous phase transition (ΔG_{pt}). The designations of regions (1–5) see in text

It was shown that the crystal nanoclusters amorphization process in the inert matrices can be either accelerated (radiation damage case) or slowed-down (radiation resistance case), and the realization of any case depends namely on the situation at the nanocluster–matrix interface: as long as the compressive stresses prevail, the nanoparticles amorphizate, but under the extending stresses the defects formation becomes slow and the crystal material state still preserves. This tendency is qualitatively confirmed by the Table 3.2 data. However, in general, it is difficult to give some proper predictions basing on the results [67–69], because the considered models are characterized by many suppositions and the relevant literature information is absent.

The NMs behavior under irradiation was widely studied using MD methods (e.g., [30, 38–40, 70–81]); the following situations arising in nanostructures under bombardment with ions, neutrons and electrons have been widely described in literature.

1. Amorphization of irradiated nanocrystals in various amorphous matrices [38–40].
2. Generation of displacement cascades in Ni nanograins (L = 5 and 12 nm) irradiated with particles with energy of 5–30 keV [70].
3. Radiation-stimulated grain growth in nano-Ni (L = 5 and 10 nm) for cascade exited by particle impact with energy of 5 keV [71].
4. Unusual behavior of the interstitial atoms and SFT in damage cascades [72].
5. Evolution of nanocrystal film morphology [73].
6. Unusual behavior of NMs with BCC and FCC structure [74].
7. Unusual behavior of GBs in irradiated nanostructures as defect sinks and sources [75].
8. Generation and growth of so-called He bubbles at interfaces [76].

In these investigations, many important features of the behavior of irradiated nanostructures were exhibited, in particular, such as the main role of intergrain boundaries and TJs acting as radiation defect sinks as well as the role of the radiation-stimulated grain growth processes. Besides the nanofilm stressed state characteristics, changes in the surface roughness were studied and some interesting peculiarities were discovered (for example, in experiments with irradiated BCC and FCC structures, predominance of vacancy clusters is observed in the looser BCC structures).

From the general considerations, it is obvious that defect generation in SiC must be more complicated than in metals because of the presence of two types of mobile interstitial atoms (Si and C) and two types of low-mobile vacancies or their clusters. This situation is very attractive for various MD calculations (e.g., [30, 77–79]), because this method allows one to study the generation and growth of clusters in β-SiC, the role of GS in the process, the behavior of cascades in such systems, etc. In particular, it was strictly shown that the nanolayered stacking faults presence leads to an enhanced mobility of interstitial Si atoms [30].

A vivid example of MD application is given in Fig. 3.9, where a situation is presented in an intergrain boundary for a moment of cascade generation and the radiation defects partially release from the boundary [70]. At the PKA energy

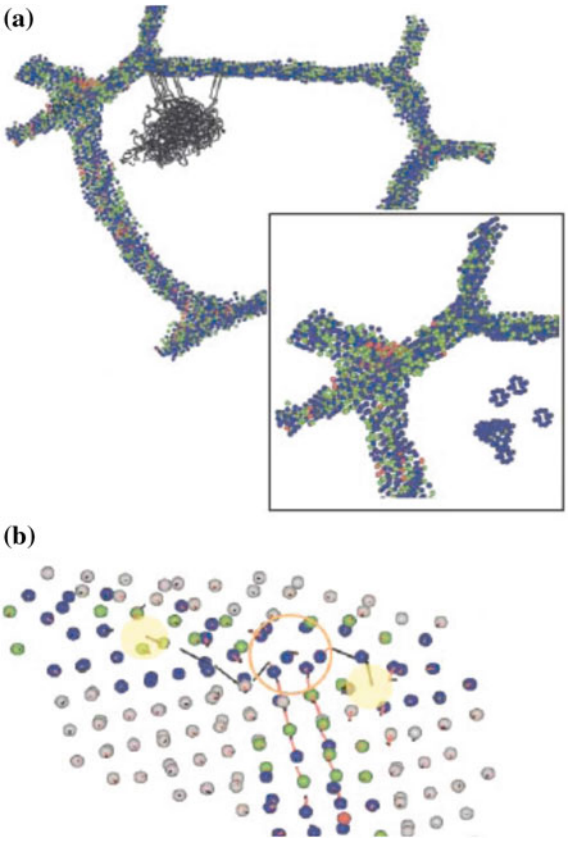

Fig. 3.9 Cross section of a grain (size of 12 nm) containing a 5 keV cascade after the PKA introduction (**a**) and scheme of GBs acting as interstitials with free volume (**b**). The *inset* shows a magnified image of the defect region after cooling (adapted from [70])

elevation, there was fixed the dislocation loops generation, and it is of interest that a process general picture is sufficiently different, when the experimental results are compared for the single crystal and nanostructured Ni samples.

In order to properly understand the effectiveness and possibilities of the MD method, let us consider in detail some results of modeling cascade formation in vanadium [80] and copper [81, 82]. The crystallites in the modeled BCC vanadium structures contain tilt and symmetric boundaries of Σ13 <320> [001] and Σ17 <410> [001] types. The number of atoms in a «calculation cell» equals 65,000–450,000 depending on the first knocked-on PKA energy in the ranges of <0.5 keV and >0.5 keV at $T = 10$ K [80]. The cascade evolution was modeled depending on its duration (more strictly, on its lifetime) for three different stages. The first one is ballistic (when the energy transferred by PKA spreads throughout the whole model object volume, and as a result the defects number achieves a maximum and thermal peaks appear). The second stage is a recombinant one (when the defects number decreases to some stable value) and the third stage is a diffusion one (further decrease in the number of defects limited to their interaction and transport processes). The main results of modeling are as follows: the presence of the large

interfaces has a pronounced effect on the development of displacement cascades; in general, they retard these processes due to accumulation of sufficient part of the radiation defects. Sometimes (depending on the PKA energy), the developed interface system can become an impenetrable barrier for a cascade development.

On the other hand, model experiments for the Frenkel pairs IAV interaction with the GBs in FCC copper allowed suggesting another mechanism of such defects annihilation, namely at first boundaries are saturated with high-mobile interstitial atoms, but then their inverse emission and absorption by the vacancies in near-boundary zones take place [81]. For a model system, presenting a combination of the special symmetric tilt boundaries of the Σ11 <110> {131} type with the total number of copper atoms in the system about 160.000 (but the number of moving atoms is of ∼130,000), the authors have simulated situations for fifteen cascades with the PKA energy of 4 keV. For the considered copper atoms system, the temperature influence on the IAV release time as well as on the inverse interstitial atoms emission was estimated. The calculation showed that within 10–15 K, the process duration is very great ($t > 10^{10}$ s!) and thus none of the proposed mechanisms works, whereas in the 70–100 K range ($t < 1$ s) the interstitial atoms play a main role and at $T = 300$ K all mechanisms work. Modeling of the concurrent processes of the radiation defects absorption by GBs and their volume recombination has shown that in the case of cascadeless copper irradiation with electrons, the vacancies accumulation from Frenkel pairs IAV on the GBs is under progress (here, the GS decreases from 40 to 15 nm) only during short time intervals, after which absorption of vacancies by coarse grains becomes a prevailing process again [82].

The complicated role of GBs in the radiation-induced defects formation and release for ion compounds was revealed in [83], where in the frame of a multi-scale MD method, the defects generation was studied near the symmetric tilt boundaries in TiO_2 at temperatures of 300 and 1000 K. On the one hand, the importance and possibilities of the MD modeling results must not be overestimated, because these methods often allow tracing only very short-lived processes, leaving many kinetic process peculiarities beyond the consideration. However, on the other hand, it is worthy to mention that the above presented results of computer simulation [81], demonstrating a non-monotonic (by temperature) character of the radiation defects release from NMs, can help to explain, at least qualitatively, some experimental data concerning the electrical resistivity of the Au foil specimens under irradiation with 60 MeV carbon ions at temperatures of 15 and 300 K (Fig. 3.10) [84].

Judging from the electrical resistivity increase, as indicated in Fig. 3.10, the nanostructured samples ($L = 23$ nm) are more sensitive to irradiation at low temperatures in comparison with their CG counterparts, i.e., in situation of the absence of radiation defect release by some above mentioned mechanisms [81]. By contrast, at room temperatures, when all of three radiation defect release mechanisms act, the nanostructured objects demonstrate a higher radiation resistance.

In general, the problems of the displacement cascades development, overlapping, interaction with interfaces, as well as their role in the radiation-induced defects release in NMs require further serious theoretical and experimental investigations.

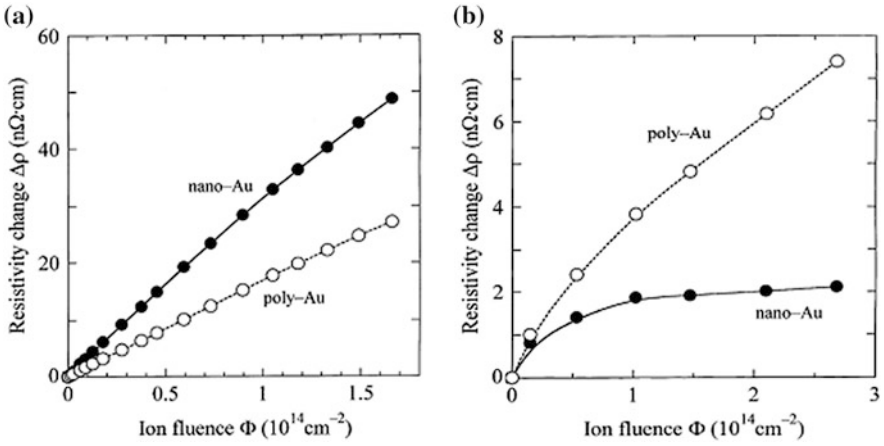

Fig. 3.10 Effect of ion fluence on the electrical resistivity increase of nano–Au (L = 23 nm) and poly–Au (annealed at 973 K for ~1 h) specimens irradiated with 60 MeV carbon ions at 15 K (**a**) and 300 K (**b**) (accepted from [84])

3.4 Examples of Applications

The main conceptions for the development of the materials, specially adapted to the new IV generation of nuclear technique, were considered in Zinkle's and Was's survey [85], where main demands were formulated for fuel, cladding, and in-core structural materials as applied to the conditions of reactor types, such as fast reactors with different liquid metal or gas cooling (such as sodium fast, lead fast, and gas fast reactors), superhigh-temperature reactors, molten salt reactors, and supercritical-water-cooled reactors with the radiation dozes up to 150–200 dpa. The proposed numerous and various demands have aroused rapid comments of the USA Los Alamos National Laboratory and Massachusetts Institute of Technology specialists [76], who underlined the NMs high tolerance to the irradiation conditions (see Tables 3.1, 3.2 and 3.3) and marked such materials perspectives, namely in connection with the conception demands [85]. First and foremost the problem is connected with nanostructured steels of the 14YWT, MA957, F95, M93, Fe–9/14/18Cr, UFG316SS, and SUS316L types developed in USA, Japan, France, and Russia (Table 3.5).

According to the matrix structure characteristics, most of these steels except for UFG316SS are only adjacent to the NMs dimension high limit ($L \sim 100$ nm), that is, a conventional value is hard to realize in practice correctly for many technological reasons. They mainly belong to the non-nickel specification of the ferritic/martensitic steel class and differ from the classic stainless steels by their low swelling at high irradiation dozes and weak activation after radiation (this factor is important for many operative post-reactor studies).

A short description of technological procedures, connected with production of these steels, is presented in Tables 3.1, 3.2 and 3.3, but a total list of procedures is

Table 3.5 Composition and characteristics of some nanostructured steels

Labeling	Type	Composition (wt%)			L_{grain} (nm)	L_{incl} (nm)
		Cr	Ni	Other elements		
14YWT [17]	Ferritic	14	–	3 W, 0.4Ti, $0.25Y_2O_3$	200–400; l = (1–5) 10^3	1–5
MA957 [62]	The same	14.3	–	0.3Mo, 0.9Ti, $0.25Y_2O_3$	n/d	1–10
F95[56, 86]	The same	12	–	2 W, 0.3Ti, $0.25Y_2O_3$	n/d	~4
M93 [56]	Ferritic/martensitic	9	–	2 W, 0.2Ti, $0.35Y_2O_3$	n/d	~4
Fe–9/14/18 Cr [87]	The same	9–18	–	1 W, ~0.3Ti, ~$0.3Y_2O_3$	~300; l ~12×10^3	2–5
SUS316L [57]	Austenitic	17	11	2.5Mo, 1.8Mn, 1TiC	100–300	–
UFG316SS [15, 58]	The same	16.6	10.6	2.25Mo, 1.1Mn, 0.7Si	40	–

complex enough, as shown in Fig. 3.11 for the Japanese F95 steel fabrication [86]. Figure 3.12 illustrates how a steel fibrous structure arises after the combination of the HE, CR and annealing. Such elongated (but shorter and narrower) grains are also characteristic for ferritic steels after HE/R treatment (14YWT, MA957, etc.), but the grains in the austenitic steels (HPT treatment) have roughly an equiaxed structure. As mentioned above, the resource of reactor tests for ferritic and austenitic nanosteels has not been rich yet. A detailed analysis of technology and properties of radiation-resistant ferritic nanosteels is presented in survey [88].

The above listed non-nickel steels are used as cladding for fuel pin in sodium fast reactors, and now they are studied as promising candidates to be used in the International Thermonuclear Experimental Reactor (ITER) and DEMO types, where the operation conditions correspond to the extreme regimes described in Zinkle's and Snead's survey [89]. Figure 3.13 demonstrates a general view of a projected fusion reactor, where at temperature of ~10^8 °C the thermonuclear synthesis of hydrogen isotopes proceeds by the mechanism:

$$^2\mathrm{D} + {}^3\mathrm{T} \rightarrow {}^3\mathrm{He}\ (3.5\ \mathrm{MeV}) + n(14.1\ \mathrm{MeV}) \tag{3.2}$$

with energy release and formation of fast helium ions and neutrons.

It is clear from Fig. 3.13 that the most intensive irradiation zone is so-called blanket (the first wall of tokomak), where the fast neutrons generated in plasma by reaction (3.2) are cooled and their energy transforms to heat, which must be released (and used!) by an abstraction system. Herein, the thermal loads are of ~10 MW/m^2

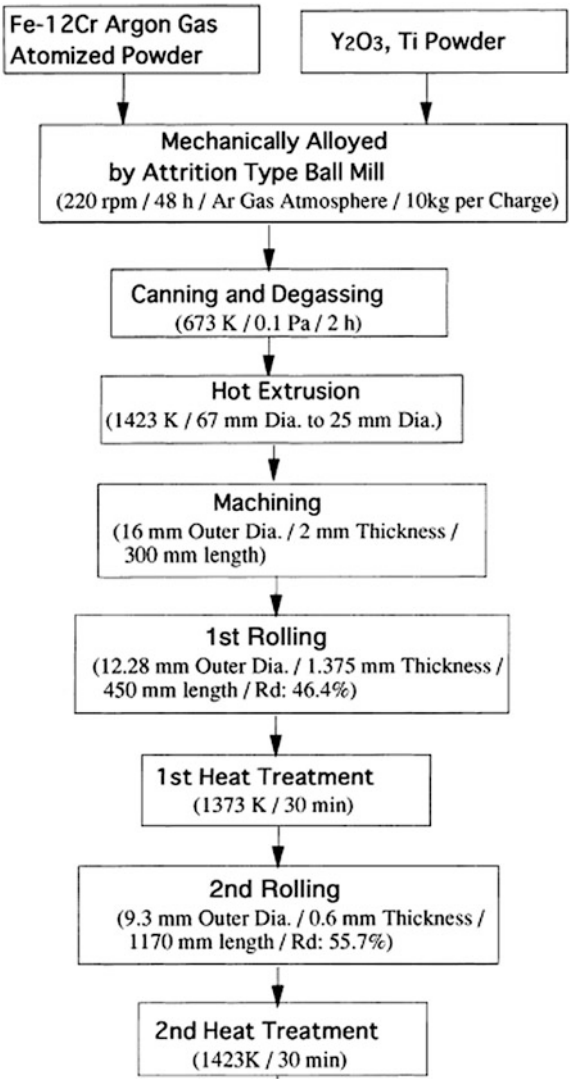

Fig. 3.11 Cladding tube manufacturing for F95 steel (adapted from [86])

and the irradiation doses can achieve 150–200 dpa, and thus, the most convenient substance as a blanket plasma-facing material is tungsten as the most high-melting and weakly activated metal with high thermal conductivity and strength characteristics. Moreover, not only the tungsten sublimation ability and abrasive wear parameters are very low, but also the tritium isotopes absorption is low. The investigation of W samples under an intensive pulse attack of the high-energy plasma jet (with energy flow densities up to 1 MJ/m^2) has demonstrated that degradation of samples is accompanied by both the surface evaporation/fusion and the destruction of near-surface layers in depth ranges to 150–250 μm [90].

Fig. 3.12 Optical microstructure of cladding tube for F95 steel after second heat treatment (adapted from [86])

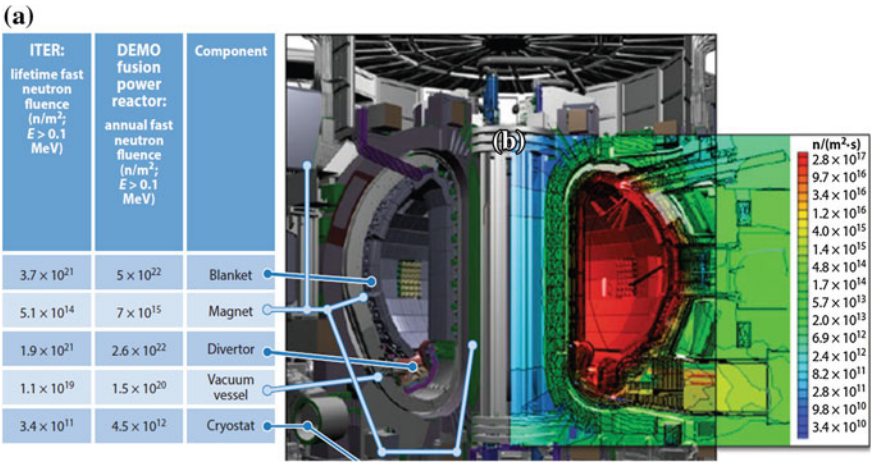

Fig. 3.13 Overview cross section of the ITER tokomak (toroidal camera with magnetic coils): **a** calculated fast neutron fluences for different key components in ITER and DEMO reactors; **b** highlights the position-dependent total neutron fluxes (adapted from [89]). The ITER reactor is now being built in Cadarache (France) with the participation of EU, Japan, USA, Russia, China, India and South Korea

Also, it should be noted that from the standpoint of using tungsten under specific operational conditions of the nuclear units, its two main shortages should be taken into account: brittleness and high value of T_{BDT}. These factors negatively influence the radiation resistance. In order to depress their role, prolonged and diversified investigations were and are carried out mainly on the basis of the nanostructure approaches. The tungsten-based materials were modified by introducing some disperse strengthening additives (such as TiC, Y_2O_3, and La_2O_3); by using various combinations of treating technological methods, such as MA, HIP, the pressure

treatment in a superplasticity state, and the formation of different laminated structured composites reinforced by W wires, etc. (e.g., [14, 91–94]). In laboratory conditions, GS was decreased to 50–200 nm, which allowed even examination of plasticity at room temperature and superplasticity at $T = 1650$ °C [92]. The neutron irradiation studies ($E > 0.1$ MeV, $T = 800$–1073 K, 0.15–0.47 dpa) of some blanket plasma-facing materials for several W alloys (with TiC additives or doped with La and K) have shown that their radiation resistance in all cases was higher than that for commonly used tungsten, but the minimum radiation hardening and the low number of radiation defects were observed namely in the UFG W–0.3TiC [93] material, which confirms the earlier obtained results presented in Tables 3.1 and 3.3 [14].

Then, it is presumed that W can be used in a diverter as a supplementary toroidal nuclear mounting part destined to remove the charged particles and blanket wear products. As an alternative promising material for diverters and blankets, the CVI SiC/SiC composites are considered because they stand out as having high radiation and thermal stability (see Fig. 3.7) [63]. Some problems concerning the transmutation processes under the materials irradiation at the nuclear fusion reactor environment are considered in [95].

Various SiC-based materials are also used in other fields of nuclear technologies, for example, as so-called TRISO-coated fuel UO_2 microparticles in superhigh-temperature gas-cooled reactors. Such 30–40 μm thick coatings are applied through CVD method in fluidized-bed layers and act a diffusion barrier for solid and gaseous fission products. It was shown that the minimal porosity (~ 0.04 %), related maximal hardness (~ 50 GPa), and elastic modulus (~ 340 GPa) of these coatings correspond to the deposition temperature about 1450 °C [96]. The presented mechanical properties are close to those for nanocrystalline SiC films [25, 26]. Furthermore, it is known that tubes from impregnated SiC/SiC composites (with a CVI SiC matrix) are investigated as materials promising for replacement of traditional zirconium shells of the rod-type fuel elements in the traditional thermal reactors.

It should be noted that some nanocomposites containing W, ^{10}B, Gd, Hf, Cd, TiB_2, and B_4C (i.e., highly absorptive components with a great neutron trapping cross-section) are investigated in order to create new materials for absorbing and regulative rods in the reactor control systems, as well as for radiation shielding against a neutron and γ-irradiation (e.g., [97–99]). It has been recently shown that some nanostructured luminophors (on the basis of $CaSiO_4$, Al_2O_3, and many other compounds) hold great promises for application in great dose β-radiation dosimetry [100, 101].

The above presented data clearly demonstrate the importance and possible applications of various NMs in the field under investigation as well as the necessity of the further investigations of their radiation stability. Besides, the radiation resistance data are the subject of much current interest in connection with problems of radiation shielding design to protect both the personal and element base of aerospace systems, etc. In general, the experimental and theoretical studies of these materials radiation stability remain very actual and the accumulation of information

about the NM irradiation occurs very intensively. Some of the recent most interesting results are presented below:

1. The unexpected fast grain growth in nanocrystalline ceria under 3 MeV Au ions [102];
2. Quantitative comparison of sink efficiency of Cu–Nb, Cu–V and Cu–Ni heterointerfaces for radiation point defects [103];
3. High radiation resistance of UFG 304L stainless steel ($L \sim 100$ nm), produced by ECAP technique, under 3.5 MeV Fe ion irradiation at 500 °C up to dose of 80 dpa [104];
4. Radiation tolerance of nanocrystalline Yttria stabilized Zirconia (10YSZ) increased with decreasing grain size from 220 to 25 nm (irradiation with 400 keV Kr ions up to 129 dpa) [105].
5. High irradiation resistance of nanolaminated MAX phases (Ti_3SiC_2, Ti_3AlC_2, Ti_2AlN, and so on) [106,107].

References

1. Golubov SI, Barashev AV, Stoller RE (2011) Radiation damage theory. In: Konigs R (ed) Encyclopedia of comprehensive nuclear materials. Elsevier, Amsterdam, Chap. 29
2. Rose M, Balough AG, Hahn H (1997) Instability of irradiation induced defects in nanostructured materials. Nucl Instr Meth Phys Res B 127–128:119–122
3. Misra A, Demkowicz MJ, Zhang X et al (2007) The radiation damage tolerance of ultrahigh strength nanolayered composites. JOM 52:62–65
4. Wurster S, Pippan R (2009) Nanostructured metals under irradiation. Scr Mater 60:1083–1087
5. Andrievskii RA (2010) Effect of irradiation on properties of nanomaterials. Phys Met Metallogr 110:229–240
6. Demkowicz MJ, Bellon P, Wirth BD (2010) Atomic-scale design of radiation-tolerant nanocomposites. MRS Bull 35:992–998
7. Andrievski RA (2011) Behavior of radiation defects in nanomaterials. Rev Adv Mater Sci 29:54–67
8. Perry AJ (1998) Microstructural changes in ion implanted titanium nitride. Mater Sci Eng, A 253:310–318
9. Rose M, Gorzawski G, Miche G et al (1995) Phase stability of nanostructured materials under heavy ion irradiation. Nanostruct Mater 6:731–734
10. Nita R, Schaeublin R, Victoria M (2004) Impact of radiation on the microstructure of nanocrystalline materials. J Nucl Mater 329–333:953–957
11. Nita R, Schaeublin R, Victoria M et al (2005) Effect of radiation on the microstructure and mechanical properties of nanostructured materials. Phil Mag 85:723–735
12. Shen TD, Feng Sh, Tang M et al (2007) Enhanced radiation tolerance in nanocrystalline Mg_2GaO_4. Appl Phys Lett 90:263115 (1–3)
13. Kilmametov AR, Gunderov DV, Valiev RZ et al (2008) Enhanced ion irradiation resistance of bulk nananocrystalline TiNi alloy. Scr Mater 59:1027–1030
14. Kurushita H, Kobayashi S, Nakai K et al (2008) Development of ultra-fine grained W–(0.2–0.8)wt% TiC and its superior resistance to neutron and 3 MeV He-ion irradiation. J Nucl Mater 377:34–40

15. Ettienne A, Radiguet B, Cunningham NJ et al (2011) Comparison of radiation-induced segregation in ultrafine-grained and conventional 316 austenitic stainless steels. Ultramicroscopy 111:659–663
16. Yu KY, Liu Y, Sun C et al (2012) Radiation damage in helium ion irradiated nanocrystalline Fe. J Nucl Mater 425:140–146
17. Parish CM, White RM, LeBeau JM et al (2014) Response of nanostructured ferritic alloys to high-dose heavy ion irradiation. J Nucl Mater 445:251–260
18. Fu EG, Misra A, Wang H et al (2010) Interface enabled defects reduction in helium ion irradiated Cu/V nanolayers. J Nucl Mater 407:178–188
19. Misra A, Thilly L (2010) Structural metals at extremes. MRS Bull 35:965–972
20. Gao Y, Yang T, Xue J et al (2011) Radiation tolerance of Cu/W multilayered nanocomposites. J Nucl Mater 413:11–15
21. Wang H, Gao Y, Fu E at al (2014) Irradiation effects on multilayered W/ZrO_2 film under 4 MeV Au ions. J Nucl Mater 455:86–90
22. Milosavljević M, Milinović V, Peruško D et al (2011) Stability of nano-scaled Ta/Ti multilayers upon argon irradiation. Nucl Instr Meth Phys Res B 269:2090–2097
23. Hong M, Ren F, Zhang H et al (2012) Enhanced radiation tolerance in nitride multilayered nanofilms with small period-thicknesses. Appl Phys Lett 101:153117 (1–5)
24. Yu KY, Liu Y, Fu EG et al (2013) Comparisons of radiation damage in He ion and proton irradiated immiscible Ag/Ni nanolayers. J Nucl Mater 440:310–318
25. Andrievski RA (2009) Synthesis, structure and properties of nanosized silicon carbide. Rev Adv Mater Sci 22:1–20
26. Wu R, Zhou K, Yue ChY et al (2015) Recent progress in synthesis, properties and potential applications of SiC nanomaterials. Progr Mater Sci 72:1–60
27. Leconte Y, Monnet I, Levalois M et al (2007) Comparison study of structural damage under irradiation in SiC nanostructured and conventional ceramics. Mater Res Soc Symp Proc 981: JJ07 (1–6). (MRS, Warrendale)
28. Jiang W, Wang H, Kim I et al (2009) Response of nanocrysralline 3C silicon carbide to heavy-ion irradiation. Phys Rev B 80:161301 (R) (1–4)
29. Gosset D, Audren A, Leconte Y et al (2012) Structural irradiation damage and recovery in nanometric silicon carbide. Progr Nucl Energy 57:52–56
30. Zhang Y, Ishimaru M, Varga T et al (2012) Nanoscale engineering of radiation tolerant silicon carbide. Phys Chem Chem Phys 14:13429–13436
31. Ishimaru M, Zhang Y, Shannon S et al (2013) Origin of radiation tolerance in 3C-SiC with nanolayered planar defects. Appl Phys Lett 103:033104 (1–4)
32. Meldrum A, Boatner LA, Ewing RC (2002) Nanocrystalline zirconia can be amorphized by ion irradiation. Phys Rev Lett 88:025503 (1–3)
33. Sickafus KE, Matzke H, Hartman T et al (1999) Radiation damage effects in zirconia. J Nucl Mater 274:66–77
34. Johannessen B, Kluth P, Liewellyn DJ et al (2007) Amorphization of embedded Cu nanocrystals by ion irradiation. Appl Phys Lett 90:073119 (1–3)
35. Johannessen B, Kluth P, Liewellyn DJ et al (2007) Ion-irradiation-induced amorphization of Cu nanoparticles embwddwd in SiO_2. Phys Rev B 76:184203 (1–11)
36. Kluth P, Johannessen B, Foran GJ et al (2006) Disorder and cluster formation during ion irradiation of Au nanoparticles in SiO_2. Phys Rev B 74:014202 (1–8)
37. Ridgway MC, Azevedo GM, Elliman RG et al (2005) Ion-irradiation-induced preferential amorphization of Ge nanocrystals in silica. Phys Rev B 71:094107 (1–6)
38. Djurabekova F, Backman M, Pakarinen OH et al (2009) Amorphization of Ge nanocrystals embedded in amorphous silica under ion irradiation. Instr Meth Phys Res B 267:1235–1238
39. Sprouster DJ, Giulian R., Araujo LL et al (2010) Ion irradiation induced amorphization of cobalt nanoparticles. Phys Rev B 81:1554 (1–8)
40. Krasheninnikov AV, Nordlund K (2010) Ion and electron irradiation-induced effects in nanostructured materials. J Appl Phys 107:071301 (1–70)

41. Chukalkin YuG (2013) Amorphization of oxides by irradiation of fast neutrons. Phys Solid State 55:1601–1604
42. Kaomi D, Motta AT, Birtcher RC (2008) A thermal spike model of grain growth under irradiation. J Appl Phys 104:073525 (1–13)
43. Radiguet B, Etienne P, Pareige P et al (2008) Irradiation behavior of nanostructured 316austenitic stainless steel. J Mater Sci 43:7338–7343
44. Lian J, Zhang J, Namavar F et al (2009) Ion beam-induced amorphous-to-tetragonal phase transformation and grain growth of nanocrystalline zirconia. Nanotechnology 20:245303 (1–7)
45. Marquis EA, Hu R, Rousseau T (2011) A systematic approach for the study of radiation-induced segregation/depletion at grain boundaries in steels. J Nucl Mater 413:1–4
46. Certain A, Kuchibhatla S, Shutthanandan V et al (2013) Radiation stability of nanoclusters in nanostructured oxide dispersion strengthened (ODS) steels. J Nucl Mater 434:311–321
47. Vo NQ, Chee SW, Schwen D et al (2010) Microstructural stability of nanostructured Cu alloys during high-temperature irradiation. Scr Mater 63:929–932
48. Tai K, Averback RS, Bellon Pinko VI et al (2009) Radiation-induced reduction in the void swelling. J Nucl Mater 385:228–230
49. Yang T, Huang X, Wang C et al (2012) Enhanced structural stability of nanoporous zirconia under irradiation of He. J Nucl Mater 427:225–232
50. Bringa EM, Monk JD, Caro A et al (2012) Are nanoporous materials radiation resistant? Nano Lett 12:3351–3355
51. Yu KY, Bufford D, Chen Y et al (2013) Basic criteria for formation of growth twins in high stacking fault energy metals. Appl Phys Lett 103:181903 (1–5)
52. Yu KY, Bufford D, Sun C et al (2013) Removal of stacking-fault tetrahedra by twin boundaries in nanotwinned metals. Nat Commun 4:1377–1384
53. Yu KY, Bufford D, Khatkhatay F et al (2013) In situ studies of irradiation-induced twin boundary migration in nanotwinned Ag. Scr Mater 69:385–388
54. Han W, Fu EG, Demkowicz MJ et al (2013) Irradiation damage of single crystal, coarse-grained, and nanograined copper under helium bombardment at 450 °C. J Mater Res 28:2763–2769
55. Wang H, Gao Y, Fu E et al (2013) Effect of high fluence Au ion irradiation on nanocrystalline tungsten film. J Nucl Mater 442:189–194
56. Yamashita S, Akasaka N, Ohnuki S (2004) Nano-oxide particle stability of 9–12Cr grain morphology modified ODS steels under neutron irradiation. J Nucl Mater 329–333:377–381
57. Matsuoka H, Yamasaki T, Zheng YJ et al (2007) Microstructure and mechanical properties of neutron-irradiated ultra-fine-grained SUS316L stainless steels and electrodeposited nanocrystalline Ni and Ni–W alloys. Mater Sci Eng, A 449–451:790–793
58. Pareige P, Etienne A, Radiguet B (2009) Experimental atamic scale investigation of irradiation effects in CW 316SS and UFG-CW 316SS. J Nucl Mater 389:259–264
59. McClintock DA, Hoelzer DT, Sokolov MA et al (2009) Mechanical properties of neutron irradiated nanostructured ferritic alloy 14YWT. J Nucl Mater 386–388:307–311
60. McClintock DA, Sokolov MA, Hoelzer DT et al (2009) Mechanical properties of irradiated ODS-EUROFER and nanocluster strengthened 14YWT. J Nucl Mater 392:353–359
61. Nanstad RK, McClintock DA, Hoelzer DT et al (2009) High temperature irradiation effects in selected Generation IV structural alloys. J Nucl Mater 392:331–340
62. Miller MK, Hoelzer DT (2011) Effect of neutron irradiation on nanoclusters in MA957 ferritic alloys. J Nucl Mater 418:307–310
63. Katoh Y, Nozawa T, Snead LL et al (2011) Stability of SiC and its composites at high neutron fluence. J Nucl Mater 417:400–405
64. Shamardin VK, Goncharenko YD, Bulanova TM et al (2012) Effect of neutron irradiation on microstructure and properties of austenitic AISI 321 steel, subjecting to equal-channel angular pressing. Rev Adv Mater Sci 31:167–173
65. Alsabbagh A, Valiev RZ, Murty KL (2013) Influence of grain size on radiation effects in a low carbon steel. J Nucl Mater 443:302–310

66. Koyanagi T, Shimoda K, Kondo S et al (2014) Irradiation creep of nanopowder sintered silicon carbide at low neutron fluences. J Nucl Mater 455:73–80
67. Ovid'ko IA, Sheinerman AG (2005) Irradiation-induced amorphization processes in nanocrystalline solids. Appl Phys A 81:1083–1088
68. Shen TD (2008) Radiation tolerance in a nanostructure: is a smaller better? Nucl Instr Meth Phys Res B 266:921–925
69. Oksengendler BI, Turaeva NN, Maximov SE et al (2010) Peculiarities of radiation-induced defect formation in nanocrystals imbedded in a solid matrix. J Exp Theor Phys 111:415–420
70. Samaras M., Derlet PM, Van Swygenhoven H et al (2002) Computer simulation of displacement cascades in nano crystalline Ni. Phys Rev Lett 88:125505 (1–4)
71. Voegeli W, Albe K, Hahn H (2003) Simulation of grain growth in nanocrystalline nickel induced by ion irradiation. Nucl Instr Meth Phys Res B 202:230–235
72. Samaras M, Derlet PM, Van Swygenhoven H et al (2003) SIA activity during irradiation of nanocrystalline Ni. J Nucl Mater 323:213–219
73. Mayr SG, Averback RS (2003) Evolution of morphology in nanocrystalline thin films during ion irradiation. Phys Rev B 68:075419 (1–9)
74. Samaras M, Derlet PM, Van Swygenhoven H et al (2006) Atomic scale modeling of the primary damage state of irradiated FCC and BCC nanocrystalline metals. J Nucl Mater 351:47–55
75. Millet PC, Aidhy DS, Desai T et al (2009) Grain-boundary source/sink behavior for point defect: an atomistic simulation study. Int J Mater Res 100:550–555
76. Beyerlein IJ, Caro A, Demkowicz et al (2013) Radiation damage tolerant nanomaterials. Mater Today 16:443–449
77. Morishita K, Watanabe Y, Kohyama A et al (2009) Nucleation and growth of vacancy-clusters in β-SiC during irradiation. J Nucl Mater 386–388:30–32
78. Swaminathan N, Kamenski PJ, Morgan D et al (2010) Effects of grain size and grain boundaries on defect production in nanocrystalline 3C-SiC. Acta Mater 58:2843–2853
79. Jiang H, Jiang C, Morgan D et al (2014) Accelerated atomistic simulation study on the stability and mobility of carbon tri-interstitial cluster in cubic SiC. Comp Mater Sci 89:182–188
80. Psakhie SG, Zolnikov KP, Kryzhevich DS et al (2009) Evolution of atomic collision cascade in vanadium crystal with internal structure. Crystal Rep 54:1002–1011
81. Bai X-M, Voter AF, Hoagland RG et al (2010) Efficient annealing of radiation damage near grain boundaries via interstitial emission. Science 327:1631–1634
82. Yang Y, Huang H, Zinkle SJ (2010) Anomaly in dependence of radiation-induced vacancy accumulation on grain size. J Nucl Mater 405:261–265
83. Bai X-M, Uberuaga BP (2012) Multi-timescale investigation of radiation damage near TiO_2 rutile grain boundaries. Phil Mag 92:1469–1498
84. Chimi Y, Iwase A, Ishikawa N et al (2001) Accumulation and recovery of defects in ion-irradiated nanocrystalline gold. J Nucl Mater 297:355–357
85. Zinkle SJ, Was GS (2013) Materials challenges in nuclear energy. Acta Mater 61:735–758
86. Ukai S, Mizuta S, Yoshitake T et al (2000) Tube manufacturing and characterization of oxide dispersion strengthened ferritic steels. J Nucl Mater 283–287:702–706
87. Dubuisson P, Carlan Y, Garat V et al (2012) ODS ferritic/martensitic alloys for sodium fast reactor fuel pin cladding. J Nucl Mater 428:6–12
88. Odette GR, Alinger MJ, Wirth BD (2008) Recent developments in irradiation-resistant steels. Annu Rev Mater Res 38:471–503
89. Zinkle SJ, Snead LL (2014) Designing radiation resistance in materials for fusion energy. Annu Rev Mater Res 44:241–287
90. Voronin AV, Sud'enkov YV, Semenov BN et al (2014) Degradation of tungsten under the action of a plasma jet. Tech Phys 59:981–988
91. Rieth M, Dudarev SL, Gonzales de Vicente SM et al (2013) A brief summary of the progress on the EFDA tungsten materials program. J Nucl Mater 442:173–180

92. Wurster S, Baluc N, Battabyal M et al (2013) Recent progress in R&D on tungsten alloys for divertor structural and plasma facing materials. J Nucl Mater 442:181–189
93. Efe M, El-Atwani O, Guo Y et al (2014) Microstructure refinement of tungsten by surface deformation for irradiation damage resistance. Scr Mater 70:31–34
94. Fukuda M, Hasegawa A, Tanno TS et al (2013) Property change of advanced tungsten alloys due to neutron irradiation. J Nucl Mater 442:273–276
95. Sawan ME, Katoh Y, Snead LL (2013) Transmutation of silicon carbide in fusion nuclear environment. J Nucl Mater 442:370–375
96. Kim W-J, Park JN, Cho MS et al (2009) Effect of coating temperature on properties of the SiC layer in TRISO-coated particles. J Nucl Mater 392:213–218
97. Buyuk B, Tugrul B, Akarsu AC et al (2011) Investigation on the effects of TiB_2 particle size on radiation shielding properties of TiB_2 reinforced BN–SiC composites. In: Pogrebnjak AD (ed), Nanomaterials: Applications and Properties (NAP-2011, Alushta), Ukrainian Sumy University, Sumy, vol 2, part II, pp 421–428
98. Schrempp-Koops L (2013) Size efficiency of neutron shielding in nanocomposites—a full-range analysis. Int J Nanosci 12:1350015 (1–8)
99. Kim J, Seo D, Lee BC et al (2014) Nano-W dispersed gamma radiation shielding materials. Adv Eng Mater 16:1083–1089
100. Salsah N (2011) Nanocrystalline materials for the dosimetry of heavy charged particles: a review. Rad Phys Chem 80:1–10
101. Kortov VS, Nikiforov SV, Moiseikin EVAG et al (2013) Luminescent and dosimetric properties of nanostructured ceramics based on aluminium oxide. Phys Sol State 55:2088–2093
102. Aidhy DS, Zhang Y, Weber WJ (2014) A fast grain-growth mechanism revealed in nanocrystalline ceramic oxides. Scr Mater 83:9–12
103. Mao Sh, Shu SH, Zhou J et al (2015) Quantitative comparison of sink efficiency of Cu–Nb, Cu–V and Cu–Ni interfaces for point defects. Acta Mater 82:328–335
104. Sun C, Zheng S, Wei CC et al (2015) Superior radiation-resistant nanoengineered austenitic 304L stainless steel for applications in extreme radiation environments. Sci Rep 5:7801 (1–6)
105. Dey S, Drazin JW, Wang Y et al (2015) Radiation tolerance of nanocrystalline ceramics: insight from Yttria stabilized Zirconia. Sci Rep 5:7746 (1–9)
106. Tallman DJ, Hoffman EN, Caspi EN et al (2015) Effect of neutron irradiation on select MAX phases. Acta Mater 85:132–141
107. Huang Q, Liu R, Lei G et al (2015) Irradiation resistance of MAX phases Ti_3SiC_2 and Ti_3AlC_2: characterization and comparison. J Nucl Mater 465:640–647